Journal of
Ceramic Science
and Technology

J. Ceram. Sci. Technol., **09** [3] 271-278 (2018)
DOI: 10.4416/JCST2018-00013
available online at: http://www.ceramic-science.com

Nb_2AlC-Particle-Reinforced ZrO_2-Matrix Composites

M. Stumpf[1], J. Biggemann[1], T. Fey*[1, 2], K. Kakimoto[2], P. Greil[1]

[1]Department of Materials Science (Glass and Ceramics), University of Erlangen-Nuernberg, Martensstr. 5, D-91058 Erlangen, Germany
[2]Frontier Research Institute for Materials Science, Nagoya Institute of Technology, Gokiso-cho, Showa-ku, Nagoya 466 – 8555, Japan

received February 9, 2018; received in revised form March 21, 2018; accepted April 2, 2018

Abstract

Nb_2AlC-particle-loaded ZrO_2-matrix composites were manufactured by means of pressureless sintering (PS) and spark plasma sintering (SPS) at 1300 °C. The MAX phase Nb_2AlC was synthesized based on the reaction of Nb, NbC and Al powder mixtures at 1600 °C in Ar-atmosphere. Nb_2AlC formation was confirmed with XRD and ICP-OES. Nano-particulate tetragonal 3Y-TZP powder was mixed with Nb_2AlC powder with a mean particle size of 7.93 µm up to a volume fraction of 19.5 %. While the microstructure of the PS composites revealed a residual porosity of 20 – 22 %, almost dense materials with a residual porosity ≤ 2.35 % were obtained by means of SPS. With increasing Nb_2AlC fraction a significant improvement of the mechanical properties was observed. An increase in fracture toughness of up to 46 % (PS) and 67 % (SPS) measured on composites loaded with 19.5 vol% Nb_2AlC compared to pure 3Y-TZP was attributed to crack bridging of Nb_2AlC particles which, depending on the orientation, may attain high strain values owing to basal slip and kink band formation.

Keywords: Nb_2AlC, ZrO_2, particle composite, toughness

I. Introduction

Particle reinforcement is an important microstructure design concept for optimizing the toughness of engineering ceramics. Brittle ceramic matrix composites reinforced with homogeneously dispersed inclusion particles may trigger energy dissipation mechanisms associated with crack propagation including bridging, deflection and shielding [1]. The dispersion of transformable tetragonal ZrO_2 particles was successfully demonstrated to yield composites with enhanced toughness in a large number of brittle oxide as well as non-oxide ceramic matrix systems [2]. Non-transformable ceramic particles with a thermal expansion coefficient higher than the matrix are able to induce residual compressive misfit stresses in the matrix upon cooling from sintering temperature which result in a pronounced toughening effect [3]. Crack bridging based on plastic deformation of ductile metal particles behind the tip of a propagating crack is another important energy-dissipative mechanism, which leads to a pronounced improvement of fracture toughness in brittle ceramic matrix systems including nano-composite materials [4, 5].

Ternary carbides $M_{n+1}AX_n$ with M = (Ti, Nb, V,…), A = (Al, Si, Sn…) and X = (C, N), called MAX phases, offer a novel option for reinforcement of ceramic matrix composites. A unique periodic alteration of high- and low-electron density regions in their hexagonal crystal structure allow the nano-laminate MAX phases to combine properties of ceramics such as high stiffness and low thermal expansion with properties of metals like enhanced damage resistance and ductility at elevated temperatures as well as at room temperature [6, 7]. Furthermore, some ternary carbides such as Ti_3AlC_2, Ti_2AlC, Ti_2SnC and Cr_2AlC have been demonstrated to exhibit efficient crack healing capability in air atmosphere by filling surface cracks with their solid oxidation products [8]. It seems to be a very attractive prospect to combine enhanced toughness with crack healing capability in novel MAX-phase-reinforced ceramic-matrix composites in order to attain higher failure tolerance, reliability and longer lifetime compared to monolithic materials.

We propose the 211 MAX phase Nb_2AlC to serve as a reinforcing filler in ZrO_2-matrix composites, which are envisaged for the next generation of thermal protection coatings on metallic gas turbine components operating at elevated temperatures > 1000 °C. Nb_2AlC is characterized by a density of 6.54 g/cm^3, a hardness of 6.1 GPa, a Young's modulus of 280 – 290 GPa, a Poisson constant of 0.257, a mean thermal expansion coefficient of 8.1 x 10^{-6}/K, a bending strength of 440 MPa, and a fracture toughness of 5.9 MPa·m$^{0.5}$ [9 – 12]. Theoretical *ab initio* calculations predict an unusually high value of ideal shear strength in the basal plane of 44.5 GPa, which can give rise to large shear strain in the basal slip system [13]. Depending on the orientation of the nano-laminate crystal structure to the crack opening stress, ductile deformation behavior even at room temperature can offer very attractive potential for

* Corresponding author: tobias.fey@fau.de

Nb_2AlC-particle reinforcement of ceramic-matrix systems.

In this work we report on the synthesis of Nb_2AlC powder and manufacturing of 3Y-ZrO_2 (tetr) composites loaded with up to 19.5 vol% Nb_2AlC. Compaction to almost fully dense materials was achieved by means of pressure-assisted spark plasma sintering (SPS) as demonstrated for the Ti_3SiC_2-loaded 3Y-TZP composite system earlier [14], but a pressureless approach has not been yet reported. To take account of the porous microstructure of plasma-sprayed coating layers typical for thermal protection coatings, pressureless sintering at same temperature was applied to retain a porosity level of 20 %. The mechanical properties were evaluated for composite materials of different microstructure and porosity. Emphasis was placed on the measurement of the fracture toughness and its variation with Nb_2AlC loading fraction.

II. Experimental Procedure

(1) Nb_2AlC synthesis and characterization

Nb_2AlC powder was synthesized with the high-temperature solid-state reaction method [15]. An equimolar mixture of high-purity Nb (99.4 % purity, < 325 mesh, H. C. Starck GmbH, Goslar, Germany), NbC (99.3 % purity, < 325 mesh, H.C. Starck GmbH, Goslar, Germany) and Al (99.5 % purity, < 325 mesh, Alfa Aesar GmbH, Karlsruhe, Germany) powders was dispersed in ethanol, homogenized in a tumbling mixer (Turbula, Willy A. Bachofen AG, Basel, Switzerland) for 6 h and uniaxially compacted (250 MPa) to yield powder pellets with a diameter of 25 mm. The reaction pellets were heated in flowing Ar to 1600 °C for 1 h in a BN-coated graphite crucible. The Nb_2AlC reaction product was ground and sieved to obtain a deagglomerated Nb_2AlC powder.

Crystalline phase compositions of the Nb_2AlC reaction product and of the ZrO_2-Nb_2AlC composites were analyzed with XRD (D8 Advance Eco, Bruker Corporation, Billerica, MA, USA) applying monochromatic CuKα radiation. The Nb:Al ratio in the MAX phase reaction product was determined by means of ICP-OES (Spectro Genesis, Spectro Analytical Instruments GmbH, Kleve, Germany). The density of the powder was measured by means of He pycnometry (AccuPyk II 1340, Micromeritics Instrument Corporation, Norcross, GA, USA). The particle size distribution of the Nb_2AlC powder was analyzed with laser light scattering (Mastersizer 2000, Malvern Instruments Ltd., Malvern, UK).

(2) Manufacturing of Nb_2AlC-loaded ZrO_2 composites

Nb_2AlC-loaded ZrO_2-matrix composites were prepared from a tetragonal ZrO_2 powder stabilized with 3 mol% Y_2O_3 (TZ-3Y-E, Tosoh Corporation, Tokyo, Japan, particle size 40 nm). The fine powder with a mean agglomerate size of 220 nm determined by means of dynamic light scattering (Nano-phox, Sympatec GmbH, Clausthal-Zellerfeld, Germany) contained 0.25 wt% Al_2O_3 as sintering aid. Powder mixtures with 0 vol%, 6.5 vol%, 13 vol% and 19.5 vol% Nb_2AlC were dispersed in ethanol (solvent) and oleic acid (dispersant) and homogenized for 4 h in a tumbling mixer. The dried specimens with a plate geometry (50 mm x 50 mm x 5 mm) were cold isostatically pressed with the application of a pressure of 180 MPa. One set of specimens was pressureless-sintered at 1300 °C for 1 h in an alumina tube furnace under flowing argon atmosphere. Another set of specimens was compacted by means of spark plasma sintering (SPS 515S, Fuji Electronic Industrial Co., Ltd, Fujimi, Japan). A uniaxial pressure of 80 MPa was applied during sintering for 8 min at the same temperature. While slow heating and cooling rates of 5 K/min were applied for PS, significantly faster rates of 80 K/min resulted in very short cycles for SPS.

(3) Microstructure and mechanical properties characterization

The microstructures of surface-polished specimens were analyzed on a FESEM (Helios Nano-lab 600i, FEI Company, Hillsboro, OR, USA). ZrO_2-matrix particle size and residual pore size were derived from image analysis of the SEM micrographs of thermally etched (1000 °C) specimens. The Young's modulus was determined by measuring the longitudinal sound velocity according to DIN EN 843 – 2. The samples (10 mm x 10 mm x 2 mm (SPS) and 2.5 mm x 2 mm x 25 mm (PS)) were immersed in water and measured in transmission with broadband frequencies from 0.5 to 15 MHz with H2K immersion probes (USD10, Krautkrämer Branson, Hürth, Germany). For calculation of the Young's modulus, values of the density of 6.54 g/cm^3 (Nb_2AlC) and 6.03 g/cm^3 (tetr. 3Y-ZrO_2) and of the Poisson ratio of 0.257 (Nb_2AlC) and 0.31 (tetr. 3Y-ZrO_2) were applied. The immersion probe delay was detected without the sample and subtracted from the ultrasonic transmit signal.

Specimens of a rectangular bar shape with dimensions of 2.5 mm x 2 mm x 25 mm were prepared by means of diamond cutting and polishing (1 µm) for measurement of the modulus of rupture based on three-point bending with a support distance of 20 mm (5565, Instron GmbH, Pfungstadt, Germany). A constant crosshead speed of 0.5 mm/min was applied. After preparation of a Vickers indent applying an indent load F of 98.1 N, the fracture toughness values were calculated according to the method of Anstis *et al.* [16]

$$K_{IC} = 0.016 \left(\frac{E}{H}\right)^{\frac{1}{2}} \cdot \frac{F}{c^{\frac{3}{2}}} \qquad (1)$$

from the measured values of hardness H, Young's modulus E, and indent crack length c. Mean values were derived from a minimum of ten measurements.

III. Results

(1) Nb_2AlC synthesis

During annealing of the Nb, NbC, Al powder pellets to 1600 °C, Nb_2AlC was formed as the major reaction product. Evaporation of Al caused the formation of a thin layer of NbC on the pellet surface which was completely removed mechanically with SiC grinding paper (d_{50} = 30 µm) prior to milling. ICP-OES analysis revealed a Nb:Al ratio of 2:1.04, which indicates an almost stoichiometric Nb_2AlC composition. XRD analysis confirmed the formation of the 211 MAX phase Nb_2AlC

with negligible fractions of the 413 MAX phase Nb_4AlC_3, Fig. 1a. The Nb_2AlC powder is characterized by a density of 6.54 g/cm³, which equals the theoretical value derived from *ab initio* calculations [10]. After grinding and sieving, a Nb_2AlC powder with a mean particle size of $d_{50} = 7.9$ µm ($d_{10} = 2.7$ µm, $d_{90} = 22.8$ µm) was obtained. The Nb_2AlC particles are faceted and exhibit characteristic nano-laminate microstructure, Fig. 2. Kink band formation [3] caused by extensive deformation of the particles during the grinding process was frequently observed.

(2) Composite sintering

Pressureless sintering of 3Y-TZP was reported to require temperatures up to 1500 °C to achieve a fractional density exceeding 95 % [17]. The sintering temperature of the Nb_2AlC-loaded ZrO_2-composites, however, was limited to 1300 °C to avoid interface reactions between the inclusion particles and the matrix. The pressureless-sintered microstructures revealed a ZrO_2-matrix grain size of 175 nm and retained a high level of porosity of ~ 20 % (0 vol% Nb_2AlC) to ~ 22 % (19.5 vol% Nb_2AlC) with a mean pore size of 170 nm. This level of porosity lies in the range of porosity (10 – 25 %) found in thermally sprayed ZrO_2-based thermal protection layers, which benefit from reduced heat conductivity compared to dense microstructures [18]. In contrast, pressure-assisted spark plasma sintering at the same temperature but with a very short dwell period of 8 min generated almost fully dense materials with a low residual porosity of 0.36 % (0 vol% Nb_2AlC) to 2.35 % (19.5 vol% Nb_2AlC) and a slightly smaller matrix grain size of 160 nm. The slight increase in porosity observed with increasing amount of Nb_2AlC may be contributed to constrained sintering phenomena with the large Nb_2AlC particles (7.9 µm) retarding the densification rate of the fine-grained ZrO_2 matrix [19].

The pronounced differences in densification behavior correspond to a different microstructure evolution. While in SPS samples no other phases than tetr.-ZrO_2 and Nb_2AlC were detected, Fig. 1b, PS specimens revealed a small fraction of additional niobium carbides, Fig. 1c.

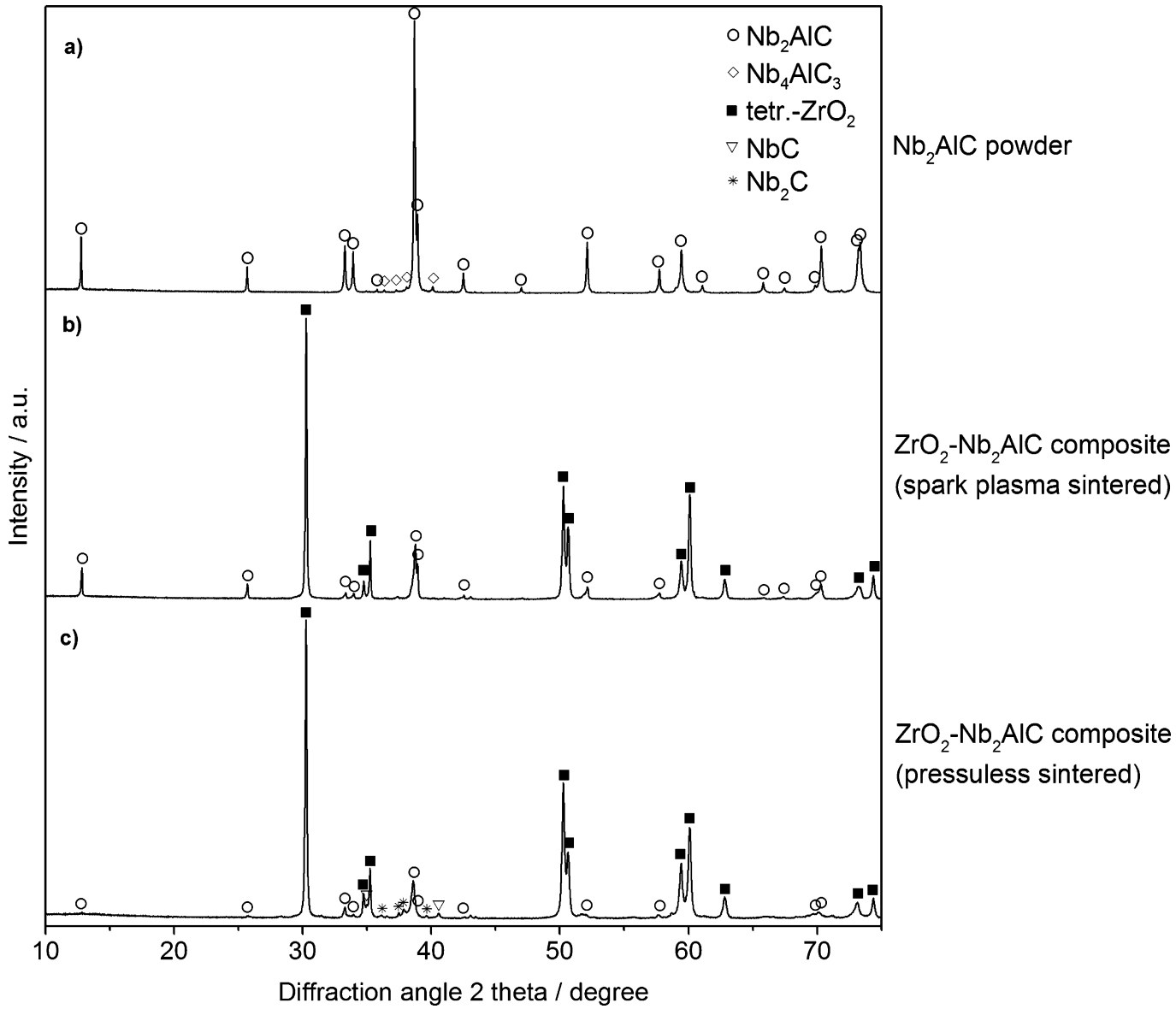

Fig. 1: XRD pattern of the synthesized Nb_2AlC powder (a) and the ZrO_2 composite loaded with 19.5 vol% (b, c).

In contrast to the dense microstructure of SPS material, the interconnected porosity of approximately 20 % of PS composites is supposed to facilitate evaporation of Al. During prolonged sintering at 1300 °C decomposition of the MAX phase may occur

$$Nb_2AlC \rightarrow (1\text{-}m)\ Nb_2C + 2m\ NbC_{1-x} + Al\uparrow \quad (2a)$$

$$Nb_2AlC \rightarrow (1\text{-}m)\ Nb_2C + m/2\ Nb_4C_{3-x} + Al\uparrow \quad (2b)$$

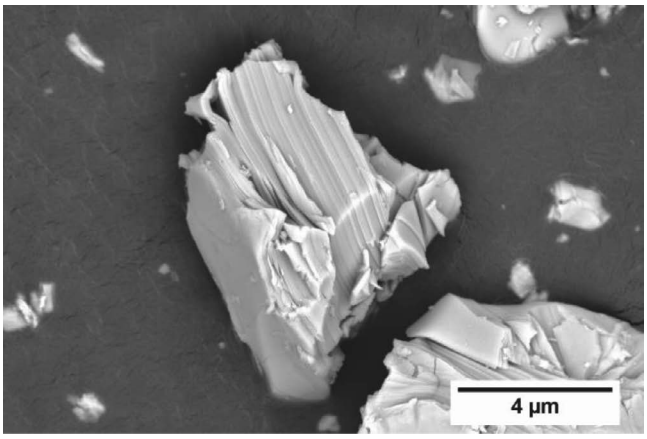

Fig. 2: SEM micrograph of a typical nano-laminate microstructure of an Nb_2AlC powder particle.

The binary Nb-C phase diagram shows the homogeneity range of the Nb_2C phase field to be less than 1 – 2 at% C at 1300 °C. Nb_4C_{3-x} and NbC_{1-x} solid solution phases with broader variation of composition ($x = 0 - 0.3$) due to defects in the carbon sub-lattice were postulated to coexist with Nb_2C [20]. While Nb_2C could be clearly identified from the XRD patterns, the low intensities and broad line widths did not allow identification of the specific carbon-deficient solid-solution phase.

Fig. 3 shows the composite microstructures of surface-polished PS and SPS specimens loaded with 19.5 vol% Nb_2AlC. Although a homogeneous distribution of the Nb_2AlC particles (bright contrast) is obvious, agglomerates of Nb_2AlC with diameters up to 100 µm could be frequently observed in both series of specimens. Only very few larger pores (black contrast) were present in the PS specimen, whereas no large pores can be seen in the SPS sample.

Since the mean coefficient of thermal expansion α of Nb_2AlC ($8.1 \cdot 10^{-6}$ / K) [9] is lower than that of the ZrO_2 matrix ($11.5 \cdot 10^{-6}$ / K) [21], thermal misfit stresses will develop upon cooling from sintering temperature to room temperature. For low particle loading fractions, Selsing's relation [22]

$$\sigma^h = \left(\alpha_{Nb_2AlC} - \alpha_{ZrO_2}\right)\Delta T \left(\frac{1+\nu_{ZrO_2}}{2E_{ZrO_2}} + \frac{1-2\nu_{Nb_2AlC}}{E_{Nb_2AlC}}\right)^{-1} \quad (3)$$

predicts a residual compressive stress of magnitude σ^h to develop inside a Nb_2AlC particle upon cooling.

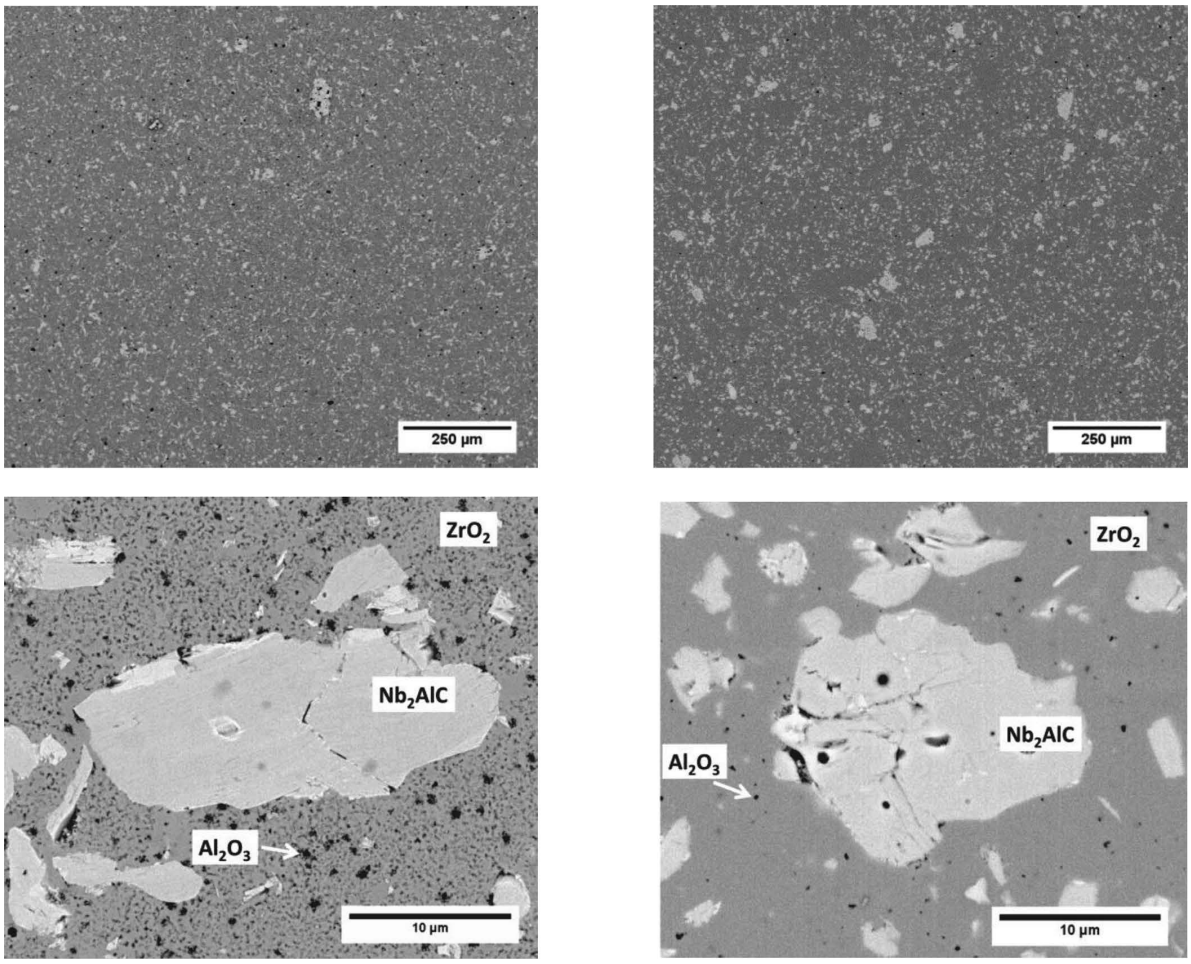

Fig. 3: SEM micrographs of ZrO_2/Nb_2AlC composites prepared with pressureless sintering (left) and spark plasma sintering (right), respectively, the Nb_2AlC particle filler, ZrO_2 matrix and Al_2O_3 sintering aid are marked in the high-resolution micrographs.

The radial compression σ_r and tangential tension σ_t in the ZrO_2-matrix in a distance r from the inclusion center of radius R are given as

$$\sigma_r = \sigma^h \left(\frac{R}{r}\right)^3 \quad \text{and} \quad \sigma_t = -\tfrac{1}{2}\,\sigma^h \left(\frac{R}{r}\right)^3 \qquad (4)$$

MAX phases exhibit a brittle-ductile transition at temperatures between 800 – 1100 °C [23]. Furthermore, a characteristic temperature of 800 – 1050 °C was reported for tetragonal ZrO_2 [24, 25] above which viscous deformation or lattice diffusion may cause stress relaxation. Hence, the effective temperature difference ΔT for stress freezing is supposed to be lower than the sintering temperature. For example, for ΔT = 800 °C (elastic properties of the ZrO_2-matrix: Young's modulus E_{ZrO_2} = 220 GPa (SPS)/106 GPa (PS), Poisson constant ν_{ZrO_2} = 0.31 and the Nb_2AlC particle inclusions: E_{Nb_2AlC} = 280 GPa, ν_{Nb_2AlC} = 0.257), Eq. (4) predicts compressive residual stresses within the Nb_2AlC particle of – 600 MPa (SPS) and – 300 MPa (PS), respectively. In the surrounding ZrO_2-matrix a radial compressive stress of same magnitude but a tangential tensile stress of half magnitude in the ZrO_2 matrix fall off as $1/r^3$. The moderate magnitudes of the maximum tangential tensile matrix stress at the interface ($R = r$) of 300 MPa (SPS) and 150 MPa (PS), respectively, seem to be below the threshold stress required for spontaneous micro-crack formation, which was confirmed by the experimental observation of crack-free microstructures.

(3) Mechanical properties

The dispersion of Nb_2AlC filler particles in the 3Y-ZrO_2 matrix leads to a significant decrease in the crack lengths that were introduced in the polished samples via Vickers indentation, Fig. 4a and b. Analysis of high magnification micrographs revealed that the indent fracture propagated in a mixed inter- and intra-granular mode depending on the orientation of the Nb_2AlC particles to the crack path. While the indent crack in the nano-sized tetragonal ZrO_2 matrix is characterized by a flat path, Nb_2AlC particle loading leads to deflection from the collinear propagation direction and a pronounced reduction in crack length. Nb_2AlC particles bridging the crack wake could be frequently observed, Fig. 4c and d. Depending on the orientation of the Nb_2AlC particle in the crack plane, a zig-zag crack path triggered by the nano-laminate particle microstructure was often observed. Furthermore, kink band formation, as displayed in Fig. 4d, indicates a non-brittle ductile deformation behavior unique for the group of nano-laminate MAX phase materials [6]. In contrast to brittle particle inclusions the rigid-plastic deformation capability of Nb_2AlC particles is expected to reduce the crack opening stress by crack bridging, which is considered as an effective mechanism for achieving enhanced work of fracture and fracture toughness in a brittle ceramic matrix composite [1, 4].

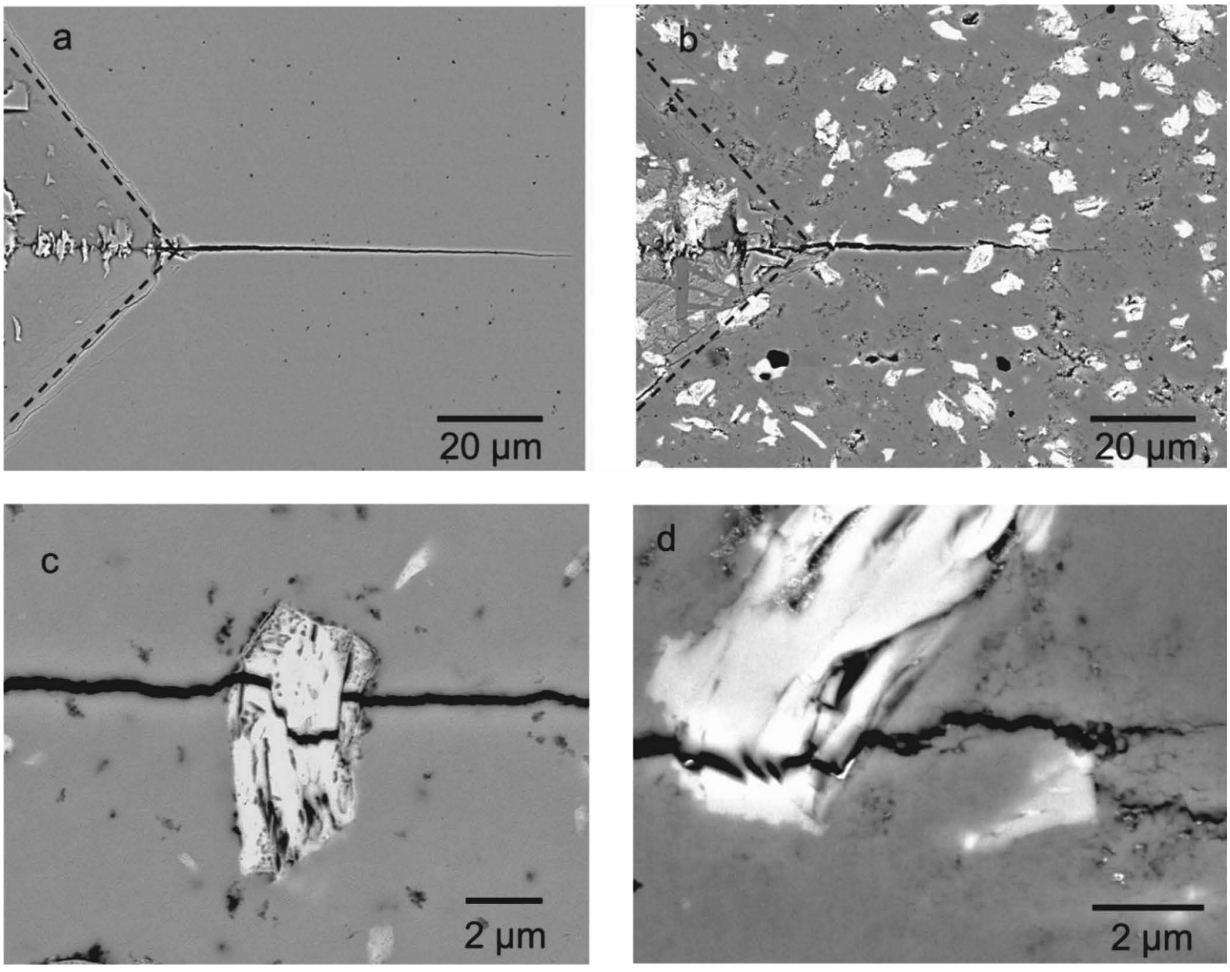

Fig. 4: SEM micrographs of crack propagation in SPS ZrO_2-matrix composites: 0 vol% Nb_2AlC (a); 19.5 vol% Nb_2AlC (b); crack bridging of Nb_2AlC inclusion particles (c) and (d).

Table 1: Mechanical properties of PS and SPS specimens with different Nb_2AlC loading.

PS – 1300 °C, 1 h	Nb_2AlC content (vol%)			
	0	6.5	13	19.5
Porosity (%)	19.8 ± 1.02	21.8 ± 0.76	20.0 ± 1.18	21.9 ± 1.00
Hardness HV10 (GPa)	5.6 ± 0.2	5.3 ± 0.2	5.5 ± 0.3	4.5 ± 0.4
Young´s modulus (GPa)	106 ± 4.2	107 ± 7.0	114 ± 4.9	104 ± 3.8
Indent crack length (μm)	319 ± 3	283 ± 9	269 ± 12	266 ± 20
Modulus of rupture (MPa)	291 ± 36	319 ± 14	330 ± 55	273 ± 26
Toughness (MPa·m$^{0.5}$)	3.4	4.2	4.6	4.9
SPS - 1300 °C, 8 min	Nb_2AlC content (vol%)			
	0	6.5	13	19.5
Porosity (%)	0.36 ± 0.22	1.67 ± 0.48	1.62 ± 0.46	2.35 ± 0.62
Hardness HV10 (GPa)	14.2 ± 0.3	14.0 ± 0.6	13.2 ± 0.9	11.5 ± 0.8
Young´s modulus (GPa)	219 ± 0.7	218 ± 1.6	218 ± 0.9	219 ± 5.0
Indent crack length (μm)	286 ± 14	236 ± 16	220 ± 14	219 ± 15
Modulus of rupture (MPa)	1030 ± 67	534 ± 21	478 ± 17	620 ± 48
Toughness (MPa·m$^{0.5}$)	3.6	4.8	5.5	6.0

The trends of mechanical property variation with increasing Nb_2AlC loading fraction are presented in Table 1. Compared to the high hardness of 3Y-ZrO_2 of 13 – 14 GPa [21], single-phase Nb_2AlC is characterized by a lower hardness of 6.1 GPa [11], giving rise to a slight decrease in hardness with increasing MAX phase content. No significant variation of the Young's modulus with increased Nb_2AlC loading fraction was observed. Owing to the high residual porosity of the PS specimens, the values of Young's modulus attained only half of the values of the dense SPS materials. Similarly, the modulus of rupture of the porous PS specimens is much lower than that of the SPS specimens. While porous PS materials exhibit only a minor influence of the Nb_2AlC fraction, the high strength of SPS matrix material is reduced. A similar observation on Ti_3SiC_2-loaded 3Y-TZP composite was attributed to the large size of the platelet-like inclusions that act as critical flaws with a flaw size significantly larger than in the monolithic 3Y-TZP matrix [26].

In contrast to the modulus of strength, the fracture toughness K_{Ic} of the composites increased remarkably with increasing Nb_2AlC particle content. Compared to the ZrO_2-matrix the K_{Ic} values of the composites increased by 44 % (PS) from 3.4 to 4.9 MPa·m$^{0.5}$ and 67 % (SPS) from 3.6 to 6.0 MPa·m$^{0.5}$ for a Nb_2AlC loading fraction of 19.5 vol%, respectively, Fig. 5.

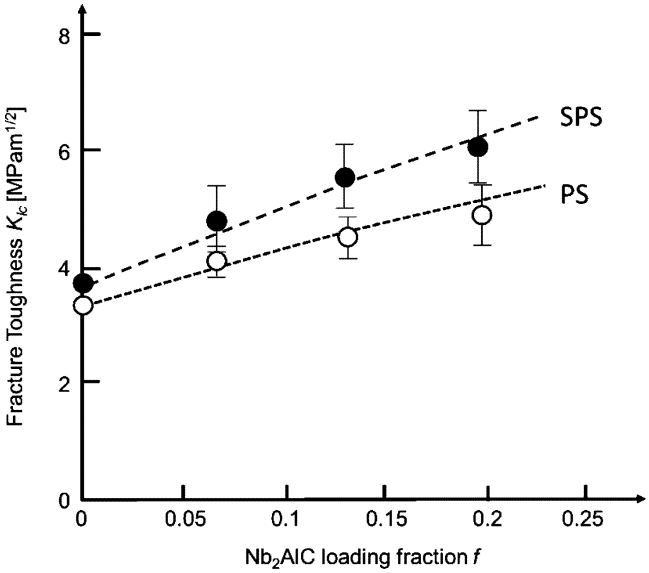

Fig. 5: Fracture toughness of ZrO_2-composites as a function of the Nb_2AlC loading fraction; dotted lines were calculated from Eq. (6).

IV. Discussion

The fracture toughness in particle-reinforced ceramic-matrix composites may be increased by crack particle interactions that induce elastic energy-dissipative mechanisms upon crack propagation. Crack front deflection (twisting and tilting) and crack shielding due to micro-cracking and tetr. to mcl. phase transformation were

considered as mechanisms dominating the toughness of ZrO_2-based ceramics [2]. In particle-reinforced composites crack bridging behind the crack front by ductile particles as well as crack shielding due to residual thermal stresses were discussed as additional mechanisms contributing to the composite toughness [3, 27]. The fracture toughness of the Nb_2AlC-loaded ZrO_2-composites $K_{Ic}$was calculated from the inherent toughness K_m of the particle-free ZrO_2-matrix and a linear addition of Nb_2AlC-particle-loading-induced fracture toughness increments $\Delta K_i(f)$ [28]

$$K_{Ic}(f) = K_m + \sum_i \Delta K(f)_i \qquad (5)$$

K_m was taken from the experimental values as 3.35 MPa $\cdot m^{0.5}$ (PS) and 3.8 MPa$\cdot m^{0.5}$ (SPS), respectively, Table 1. To a first approximation, K_m was assumed to be independent of the Nb_2AlC volume fraction f whereas particle reinforcement is represented by the mechanism-dependent toughness increments $\Delta K_i(f)$. Calculation of the toughness increment ΔK according to the micro-mechanical model for crack deflection [29] suggests only a minor contribution of approximately + 0.4 MPa$\cdot m^{0.5}$ for a Nb_2AlC loading fraction of 19.5 %, which accounts for less than 20 % of the fracture toughness increase observed experimentally. The thermal residual stress model of Taya *et al.* [3] predicts an average tensile stress in the ZrO_2 matrix upon cooling from sintering temperature which for a temperature difference of 800 °C is of the same magnitude but with a negative sign (- 0.4 MPa$\cdot m^{0.5}$) and instead a "weakening" with lower toughness is predicted [27].

A substantial toughness increase, however, can be expected from crack bridging triggered by Nb_2AlC particles in the crack wake, Fig. 6. In the MAX phase with nano-layered crystal structure (space group *P*63/*mmc*) highly mobile dislocations abundant and confined in the basal Al-metal layers are anticipated to enable basal slip and to form kink bands which as a ubiquitous micro-mechanism enable significantly larger strain and crack opening distances compared to brittle particle inclusions [6].

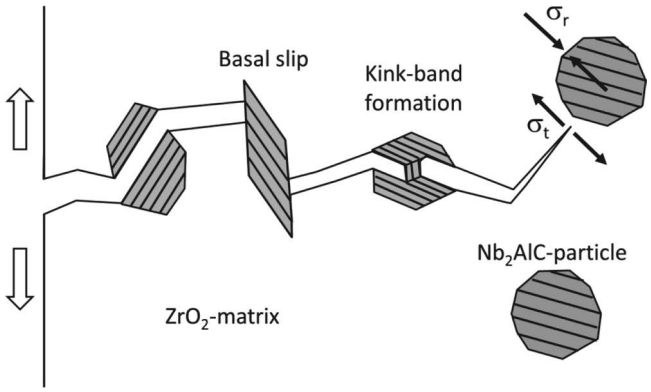

Fig. 6: Crack growth model involving crack bridging triggered by Nb_2AlC particles dispersed in the ZrO_2-matrix. Local residual thermal mismatch stresses in the ZrO_2 matrix are indicated by σt and σ_r.

For the case of rigid-plastic inclusion particles, the fracture toughness increment due to crack bridging $\Delta K_{bridging}$was derived from the small-scale particle-pinned crack model of Budiansky *et al.* [30]

$$\Delta K_{bridging} = K_m \left\{ \sqrt{1-f} \left[1 + \left(\frac{2f}{1-f} \right) \frac{E_m S \nu_p}{K_m^2 (1-\nu_m^2)} \right]^{1/2} - 1 \right\} \qquad (6)$$

Since the cohesive strength S of a Nb_2AlC particle is not known, the experimental value of the bending strength S = 440 MPa measured on hot-pressed Nb_2AlC [9] was taken for the calculation. The critical plastic crack face displacement v_p was derived by curve fitting to the experimental toughness values, Fig. 5. The fitted values of the critical plastic crack face displacement v_p of 6 x 10^{-7} m (SPS) and 4.5 x 10^{-7} m (PS), respectively, correspond to a Nb_2AlC particle strain of 7.6 % – 5.8 %. Similar magnitudes of extended strain exceeding 10 % were reported on MAX phases even at room temperature, when the basal planes are oriented such that slip occurs along the basal plane and they behave as ideal plastic solids [6]. In contrast, when the slip planes are parallel to the applied load and deformation by ordinary dislocation glide is suppressed, the MAX phase particle yields at higher stresses by kink band formation. In this case, considerable strain softening occurs because the kink bands rotate basal planes in such a way as to induce shear band formation [7].

Three-dimensional crack propagation is a complex process, some parts of the crack front propagate inside the ZrO_2 matrix, whereas other parts of the front propagate through the Nb_2AlC grains as well as along Nb_2AlC-ZrO_2 interfaces. Hence the calculations tend to overestimate the contribution of Nb_2AlC-particle crack bridging, and other toughening mechanisms like deflection [29] and micro-cracking [31] should not be neglected. Furthermore, in the vicinity of a Nb_2AlC particle, the tensile residual tangential matrix stress component may induce micro-cracking as well as tetragonal to monoclinic ZrO_2 phase transformation in the superimposed stress field of a propagating crack. The combined effect of local deflection from the collinear crack direction and the imposed transformation strain may give rise to additional crack shielding and an increased crack-growth resistance compared to the particle-free matrix material [26, 32].

V. Conclusions

3Y-TZP composites loaded with up to 19.5 vol% Nb_2AlC were synthesized by means of pressureless sintering as well as spark plasma sintering at 1300 °C. In both microstructures with high porosity (PS: 20 %) as well as low porosity (SPS: < 2.35 %), a pronounced toughening effect with increasing Nb_2AlC fraction was demonstrated. Microstructure observations as well as model calculations suggest that crack bridging triggered by the rigid-plastic Nb_2AlC particles in the crack wake contributes substantially to the improvement in fracture toughness. Combining the toughening capability with the crack-healing potential based on the formation of Nb-oxides and $NbAlO_4$ out of Nb_2AlC particles [32] is a very attractive prospect for the development of novel ZrO_2-based composites with improved failure tolerance. Hence, Nb_2AlC-reinforced ZrO_2-composites offer high potential for the development of thermal protection coatings on metal-based gas turbine components with higher reliability and longer lifetime.

Acknowledgments

Financial support from the DFG project GR961/33 – 2 is gratefully acknowledged. The authors thank H.C. Starck GmbH for providing Nb and NbC powders.

References

1 Evans, A.G.: Perspective on the development of high-toughness ceramics, *J. Am. Ceram. Soc., 73, 187 – 206, (1990).*

2 Evans, A.G., Heuer, A.H.: Review-transformation toughening in Ceramics: Martensitic transformations in crack-tip stress fields, *J. Am. Ceram. Soc.*, **63**, 241 – 248, (1980).

3 Taya, M., Hayashi, S., Kobayashi, A.S., Yoon, H.S.: Toughening of a particulate-reinforced ceramic-matrix composite by thermal residual stress, *J. Am. Ceram. Soc.*, **73**, 1382 – 1391, (1990).

4 Yeomans, Y.: Ductile particle ceramic matrix composites – scientific curiosities or engineering materials, *J. Eur. Ceram. Soc.*, **28**, 1543 – 1550, (2008).

5 Niihara, K.: New design concept of structural ceramics: Ceramic nanocomposites. *J. Ceram. Soc. Japan*., **99**, 974 – 982, (1991).

6 Radovic, M., Barsoum, M.: MAX phases bridging the gap between metals and ceramics, *Am. Ceram. Soc. Bull.*, **92**, 20 – 7, (2013).

7 Barsoum, M.W., El-Raghy, T.: Room-temperature ductile carbides, *Metall. Mat. Trans. A*, **30**, 363 – 369, (1999).

8 Greil, P.: Generic principles of crack healing ceramics, *J. Adv. Ceram.*, **1**, 249 – 267, (2012).

9 Zhang, W., Travitzky, N., Hu, C.F., Zhou, Y.C., Greil, P.: Reactive hot pressing and properties of Nb_2AlC, *J. Am. Ceram. Soc.*, **92**, 2396 – 2399, (2009).

10 Sun, Z., Li, S., Ahnya, R., Schneider, J.M.: Calculated elastic properties of M_2AlC (M = Ti, Va, Cr, Nb, and Ta), *Solid State Commun.*, **129**, 589 – 592, (2004).

11 Salama, I., El-Raghy, T., Barsoum, M.W.: Synthesis and mechanical properties of Nb_2AlC and $(Ti,Nb)_2AlC$, *J. Alloy. Compd.*, **347**, 271 – 278, (2002).

12 Barsoum, M.W., Radovic, M.: Elastic and mechanical properties of the MAX phases, *Ann. Rev. Mater. Res.*, **41**, 195 – 227, (2011).

13 Music, D., Sun, Z., Voevodin, A.A., Schneider, J.M.: *Ab initio* study of basal slip in Nb_2AlC, *J. Phys. Condens. Mat.*, **18**, 4389 – 4395, (2006).

14 Pan, W., Shi, S.L.: Microstructure and mechanical properties of Ti_3SiC_2/3Y-TZP composites by spark plasma sintering, *J. Eur. Ceram. Soc.*, **27**, 413 – 417, (2007).

15 Wang, Y.C., Liang, Z.H., Peng, G.H., Xu, J.G.: Synthesis of Nb_2AlC material by high temperature solid state reaction method, *Key Eng. Mat.*, **655**, 240 – 243, (2015).

16 Anstis, G.R., Chantikul, P., Lawn, B.R., Marshall, D.B.: A critical evaluation of indentation techniques for measuring fracture toughness: I, Direct crack measurements, *J. Am. Ceram. Soc.*, **64**, 533 – 538, (1981).

17 Chu, H.L., Wang, C.L., Lee, H.E., Sie, Y.Y., Chen, R.S., Hwang, W.S., Wang, M.C.: Effect of sintering process parameters on the properties of 3Y-PSZ ceramics, *Mat. Sci. Eng.*, **47**, 012005, (2013).

18 Kulkarni, A., Vaidya, A., Goland, A., Sampath, S., Herman, H.: Processing effects on porosity-property correlations in plasma sprayed yttria-stabilized zirconia coatings, *Mat. Sci. Eng. A*, **359**, 100 – 111, (2003).

19 Bordia, R.K., Scherer, G.W.: On constrained sintering – III. Rigid inclusions, *Acta Metall.*, **36**, 2411 – 2416, (1988).

20 Smith, J.F., Carlson, O.N.: The niobium-carbon system, *J. Nucl. Mater.,* **148**, 1 – 16, (1987).

21 Zhang, S., Zhao, D.L.: Aerospace Materials Handbook. CRC Press, Baton Rouge, FL (2013)

22 Selsing, J.: Internal stresses in ceramics, *J. Am. Ceram. Soc.*, **44**, 419, (1961).

23 Barsoum, M., Farber, L., El-Raghy, T.: Dislocations, kink bands, and room-temperature plasticity of Ti_3SiC_2, *Metall. Mater. Trans. A*, **30**, 1727 – 1738, (1999).

24 Morscher, G.N., Pirouz, P., Heuer, A.H.: Temperature dependence of hardness in yttria-stabilized zirconia single crystals, *J. Am. Ceram. Soc.*, **74**, 491 – 500, (1991).

25 Gogotsi, G.A., Ostrovoy, D.Y.: Deformation and strength of engineering ceramics and single crystals, *J. Eur. Ceram. Soc.*, **15**, 271 – 281, (1995).

26 Pan, W., Shi, S.L.: Microstructure and mechanical properties of $Ti_3SiC_2/_3$Y-TZP composites by spark plasma sintering, *J. Eur. Ceram. Soc.*, **27**, 413 – 417, (2007).

27 Ohji, T., Jeong, Y.K., Choa, Y.H., Niihara, K.: Strengthening and toughening mechanisms of ceramic nanocomposites, *J. Am. Ceram. Soc.*, **81**, 1453 – 1460, (1998).

28 Becher, P.F.: Microstructural design of toughened ceramics, *J. Am. Ceram. Soc.*, **74**, 255 – 269, (1991).

29 Faber, K.T., Evans, A.G.: Crack deflection processes - I. theory, *Acta Metall.*, **31**, 565 – 576, (1983).

30 Budiansky, B., Amazigo, J.C., Evans, A.G.: Small-scale crack bridging and the fracture toughness of particulate-reinforced ceramics, *J. Mech. Phys. Solids*, **36**, 167 – 187, (1988).

31 Evans, A.G., Faber, K.T.: Toughening of ceramics by circumferential microcracking, *J. Am. Ceram. Soc.*, **64**, 394 – 398, (1981).

32 Basu, B., Veugels, J., van der Biest, O.: Toughness tailoring of yttria-doped zirconia ceramics, *Mat. Sci. Eng. A*, **380**, 215 – 221, (2004).

33 Salama, I., El-Rhagby, T., Barsoum, M.W.: Oxidation of Nb_2AlC and $(Ti, Nb)_2AlC$ in air, *J. Electrochem. Soc.*, **150**, C152 – 158, (2003).